Journal of Materials Chemistry A

ROYAL SOCIETY OF CHEMISTRY

PAPER

View Article Online
View Journal | View Issue

Cite this: J. Mater. Chem. A, 2022, 10, 9010

On the electrochemical properties of the Fe–Ti doped LNMO material $LiNi_{0.5}Mn_{1.37}Fe_{0.1}Ti_{0.03}O_{3.95}$†

Pirmin Stüble, *[ab] Holger Geßwein,[a] Sylvio Indris,[a] Marcus Müller[a] and Joachim R. Binder[a]

Received 12th January 2022
Accepted 10th March 2022

DOI: 10.1039/d2ta00299j

rsc.li/materials-a

$LiNi_{0.5}Mn_{1.5}O_4$ (LNMO) based spinel cathode materials for lithium-ion batteries are promising alternatives to widely used mixed transition-metal layered $Li(Ni,Co,Mn)O_2$ (NCM) oxides. LNMO is cobalt free and thus cost efficient, while providing a high operating voltage of 4.7 V (*vs.* Li/Li^+) and remarkable energy density of ~650 W h kg^{-1}. Commercialization and large-scale application however are still hindered, as short cycle life remains a main issue. To help overcome this problem, we present a comprehensive investigation into Fe–Ti doped LNMO materials with the formal composition $LiNi_{0.5}Mn_{1.37}Fe_{0.1}Ti_{0.03}O_{3.95}$ (LNMFTO). Within this study, samples were calcined at temperatures between 460 °C and 940 °C and were cooled down to room temperatures rapidly or slowly. Small changes in the crystal structures were tracked by using a high-precision powder X-ray diffraction (PXRD) setup, while changes in cation order were investigated with Raman spectroscopy. It is shown that carefully elaborated calcination programs allow to maintain the optimized morphological features such as particle size, shape and specific surface, while crystallographic properties, such as the amounts of Mn(III) or (partial) cation order, can be adjusted independently. We provide experimental evidence that calcination at high temperatures leads to nickel loss in the spinel phase, but not to the formation of additional oxygen defects. LNMFTO samples show good cycling stabilities and over 98% capacity retention after 100 cycles with capacities larger than 90 mA h g^{-1} at discharge rates of 10C when cycled *vs.* lithium metal. These results are almost fully transferable to cathodes with high active material loadings cycled *vs.* graphite anodes. A capacity retention of > 89% for 500 cycles and residual capacities of >100 mA h g^{-1} are observed, which makes LNMFTO a suitable candidate for industrial applications.

1. Introduction

$LiNi_{0.5}Mn_{1.5}O_4$, referred to as LNMO, is a promising cobalt-free cathode material for lithium-ion batteries with a theoretical capacity of 147 mA h g^{-1} and a high operating voltage of 4.7 V (*vs.* Li/Li^+) corresponding to the Ni^{2+}/Ni^{4+} redox couple. LNMO provides a theoretical energy density of 650 W h kg^{-1}, hence is superior to traditional layered oxide battery materials such as $LiCO_2$.[1] The main issues are electrolyte oxidation due to high operating voltages, Mn^{3+} dissolution[2] and the poor cycle life of LNMO/graphite full cells.[3]

From the fully lithiated state, $LiNi^{II}_{0.5}Mn^{IV}_{1.5}O_4$, Li^+ can be reversibly extracted while Ni(II) is oxidized to Ni(IV), resulting in the composition $Ni^{IV}_{0.5}Mn^{IV}_{1.5}O_4$ for the fully delithiated state. LNMO can crystallize with two idealized arrangements of the transition metal ions, described as "disordered" and "ordered" spinel.[4] The latter is thermodynamically stable at room temperature[5] and crystallizes in the space group $P4_332$ with nickel and manganese ions occupying Wyckoff positions 12*d* and 4*a*, respectively. In the kinetically favored disordered state, Ni and Mn ions are distributed statistically over the occupied octahedral sites 16*d* of the space group $Fd\bar{3}m$. Lithium ions occupying tetrahedral voids in both cases are located at 8*a* sites, while oxygen in the disordered/ordered structure is located at Wyckoff positions 32*e* and 24*e*/8*c*, respectively.[6] It is assumed that most LNMO samples are neither fully ordered nor disordered, but are mixtures of both with crystal domains of varying Ni/Mn ordering schemes.[5,7–9]

Besides cation order, oxygen deficiencies are a widely accepted[6,10–14] feature of LNMO and spinel-type predecessor materials such as $LiMn_2O_4$ (LMO), allowing for conclusive explanations of specific LNMO properties. Oxygen defects are described to occur at high calcination temperatures of 650 °C, 690 °C and 730 °C in nitrogen, ambient and oxygen atmospheres[5,15] and are accompanied by a partial reduction of Mn(IV) to Mn(III)[10,11] which is necessary to maintain charge neutrality. The Mn(III) and oxygen content of LNMO materials highly depend on the thermal treatment and are affected by several

[a]Institute for Applied Materials, Karlsruhe Institute of Technology, 76344 Eggenstein-Leopoldshafen, Germany. E-mail: pirmin.stueble@kit.edu

[b]Helmholtz Institute Ulm, 89081 Ulm, Germany

† Electronic supplementary information (ESI) available. See DOI: 10.1039/d2ta00299j

parameters, such as calcination temperature and duration, partial oxygen pressure and the cooling rate.[11–13] Ordered samples calcined at 700 °C and slowly cooled to room temperature show no or only very small deviations from the ideal stoichiometry $LiNi_{0.5}Mn_{1.5}O_4$ and thus they contain Mn(IV) almost exclusively. In the temperature range of 700 °C to 950 °C, increasing numbers of oxygen defects occur and compositions like $LiNi_{0.5}Mn_{1.5}O_{4-\delta}$ with $0 \lesssim \delta \lesssim 0.7$ are described. Simultaneously, an additional redox plateau assigned to $Mn^{3+/4+}$ appears when cycling these materials.[11] Neglecting deviations in the Li, Ni and Mn content, the formal composition can therefore be described as $LiNi_{0.5}Mn^{IV}_{1.5-2\delta}Mn^{III}_{2\delta}O^{-II}_{4-\delta}$, and hereafter will be referred to as the charge balancing mechanism A. Due to the increased octahedral high spin ionic radius of Mn^{3+} compared to Mn^{4+} (64.5 pm *vs.* 53 pm),[16] oxygen non-stoichiometry manifests itself with slightly larger lattice parameters. For a more detailed discussion including coordination polyhedra and metal–oxygen bond length, the reader is referred to Pasero *et al.*[11] Until today, it has been often assumed that the cation (dis)order and oxygen nonstoichiometry are related phenomena.[1,10,15] However, there is strong evidence from several studies, that there is no direct relation between oxygen release and cation ordering.[5,11]

An alternative approach to explain the composition of LNMO materials is advocated by the Cabana group.[4,9,17] It is argued conclusively that oxygen release is a side effect of the formation of the rocksalt secondary phase, due to deviating metal to oxygen ratios (3 : 4 for LNMO *vs.* 1 : 1 for the secondary phase). The latter is rather Ni rich and frequently described as $Li_xNi_{1-x}O$, see ref. 18 and references herein, and thus, secondary phase formation must be accompanied by Ni-depletion of LNMO. The loss of Ni(II) however, requires partial reduction of Mn(IV) to Mn(III) and thus formally, the spinel phase can be described as $LiNi_{0.5-x}Mn_{1.5+x}O_4$ or, more precisely, as $LiNi^{II}_{0.5-x}Mn^{IV}_{1.5-x}Mn^{III}_{2x}O_4$. This charge balancing mechanism B thus provides an alternative explanation for the presence of Mn(III) in LNMO at higher calcination temperatures without the necessity for oxygen non-stoichiometry.

Regardless of its origin, Mn(III) is commonly believed to be disproportionate to Mn(IV) and Mn(II) and the latter one easily dissolves in the electrolyte and this plays a central role in cell degradation.[1,2] $LiNi_{0.5}Mn_{1.5}O_4$ with ideal composition, thus without significant amounts of (degradation inducing) Mn(III) or the (capacitance lowering) secondary phase is experimentally accessible by a long calcination at 700 °C. From a superficial point of view, it should therefore provide the best properties for battery applications. Practically however, most research groups find the best results when using Mn(III)-rich materials calcined between 800 °C and 900 °C, since they yield better capacities and superior cycling stabilities. Some reasons given are higher ionic[19] and electrical conductivities.[10,20] Inconsistent results are likewise found concerning the particle shape. Some authors suggested that particles of truncated octahedra, which expose {110} facets in addition to {111} facets, show superior electrochemical stabilities compared to particles with a pure octahedral shape,[21,22] even though the latter should be more stable from a thermodynamical point of view.[23]

It remains a main challenge to find and understand the reasons for such discrepancies. Therefore, as understanding progresses and research questions become more sophisticated, it has become more important to choose proper experimental conditions and keep track of the many relevant parameters simultaneously. When highlighting the effect of morphological parameters such as particle size, shape and specific surface, deviations that may arise from cathode manufacturing should not be lost sight of and, for obvious reasons, the chemical composition of the materials should not change at all.

Besides the optimization of LNMO itself, electrolyte modification[13] and the use of cell additives,[20] metal element doping is a common method to improve material properties such as conductivity, cycle stability and rate capability. In the latter approach, Li, Mn and/or Ni are substituted by doping elements such as Na, Al, Ti, Cr, Fe, Zn, and Co. Numerous studies have been published and overviews of latest developments are found in recent reviews.[1,13,24] In contrast to most prior doping studies, in the present work manganese is replaced exclusively. The doping elements Ti^{IV} and Fe^{III} both lead to an increase of the lattice parameter,[25–27] suppress the formation of cation order[25,28] and increase ionic and electronic conductivities.[28–30] Finally, titanium and iron are cheap and abundant doping elements and, as we will show, Fe–Ti doping allows for excellent electrochemical properties combined with a very low Mn(III) content, which is an unsolved problem with undoped LNMO.[17,31]

The composition $LiNi_{0.5}Mn_{1.37}Fe_{0.1}Ti_{0.03}O_{3.95}$ investigated herein, and hereafter referred to as LNMFTO, has already been investigated in an earlier study by our group.[29] But while the preceding work mainly focused on cyclability in a wider voltage range of 2 V to 5 V, the present study, primarily addresses the crystal chemistry of LNMFTO. Therefore, the influence of surface area and crystal shape and size is minimized by an appropriate choice of calcination programs. This allows to investigate the effect of variations in the Mn(III) content and cation order on the electrochemical properties independent of the morphological properties. Finally, it is shown that the application of our results could be part of a viable path towards industrialization of LNMFTO-graphite cells.

2. Experimental

2.1. Material preparation

$LiNi_{0.5}Mn_{1.37}Fe_{0.1}Ti_{0.03}O_{3.95}$ was prepared by a two-step spray-drying synthesis. The starting compounds lithium acetate ($Li(CH_3COO)\cdot 2H_2O$, 98%, Acros Organics), manganese acetate ($Mn(CH_3COO)_2\cdot 4H_2O$, >99%, Sigma-Aldrich), nickel acetate ($Ni(CH_3COO)_2\cdot 4H_2O$, 98+% Alfa Aesar), iron(III)nitrate ($Fe(NO_3)_3\cdot 9H_2O$, 98+%, Alfa Aesar), tetraisopropylorthotitanate ($C_{12}H_{28}O_4Ti$, >98%, Merck) and acetic acid (CH_3COOH, 100% anhydrous, Merck) were dissolved in distilled water. After complete dissolution, the aqueous solutions were mixed in stoichiometric ratios. Dried precursor powders were obtained by spray drying the precursor solutions. The precursor powders were then converted to the corresponding spinel oxides by a two-step calcination process. In the first step, the precursors

were calcined for two hours at 500 °C. After cooling down to room temperature, a second calcination program at 800 °C (2 h) followed. Heating and cooling rates were 300 K h^{-1}. The obtained material was subsequently mixed with three equivalents of distilled water and ground for 24 hours in a planetary ball mill (Fritsch Pulverisette 5, 3 mm ZrO_2 grinding balls) and then spray dried again. The granules obtained (hereafter referred to as A1) were then calcined at 900 °C for 20 hours, cooled to 600 °C and held at this temperature for another 30 hours. This process provided the starting material (A2) for the following investigations.

Two test series with 13 samples each were then prepared by further calcination programs with maximum temperatures ranging from 460 °C to 940 °C in steps of 40 °C. With increasing temperatures, shorter holding times were chosen, to avoid changes in morphological properties such as particle size and shape. In the first fast cooled series (samples FC460 to FC940, with numbers corresponding to the maximum temperature in °C), the specimens were cooled down quickly, with cooling rates set to 600 K h^{-1}. These fast rates, limited by the cooling rate of the furnace, were achieved for temperatures of approximately 500 °C and above. For the slow cooled series (samples SC460 to SC940), the identical maximum temperatures and holding times were applied. However, within the temperature range of 650 to 350 °C a slow cooling rate of 10 K h^{-1} was introduced. All thermal treatments were carried out in Al_2O_3 crucibles in the ambient atmosphere. A detailed overview of the individual thermal treatments can be found in Table S1 in the ESI.†

2.2. Material characterization

The particle morphologies were studied by scanning electron microscopy (SEM) with a Zeiss Supra 55 FE-SEM using acceleration voltages of 2 kV to 4 kV. Samples of the LNMFTO granule powders were fixed with carbon adhesive tape. To further investigate the core structures and the porosity of the granules, cross-sections of cathodes were prepared by ion-milling using argon-ions (TIC-3X, Leica Microsystems). For EDX-analysis an Ultim Extreme silicon drift detector from Oxford Instruments (AZtec software) was applied at a SEM acceleration voltage of 4 kV. Particle size distributions of the materials obtained from the spray drying process (A1) and after the initial calcining step (A2) were determined by a laser scattering particle size distribution analyzer LA-950 (Horiba). The granule porosity and pore size distribution of the starting material A2 were measured by mercury intrusion porosimetry with a CEI Pascal 1.05, Thermo Electron. In accordance with SEM images of the corresponding material, the granule porosity was calculated from the pore diameter < 1.5 μm and the theoretical density (4.2 g cm^{-3}). Nitrogen physical adsorption isotherms were measured with a surface area analyser Gemini VII 2390 (Micromeritics). Calculations of the specific surface were performed according to the Brunauer–Emmett–Teller (BET) theory.[32] The specific surfaces of the pristine material A2 and materials FC460 to FC940 were analysed using about 0.7 g of each sample. Prior to the measurements, the specimens and tubes were dried under vacuum at 120 °C for at least 16 h. As the material surface is considered highly unlikely to change significantly during a slow cooling process, additional measurements for the slowly cooled samples were omitted. Fe Mößbauer spectroscopy was performed in transmission mode at room temperature with a constant-acceleration spectrometer (WissEl) and a $^{57}Co(Rh)$ source. Isomer shifts are given relative to that of α-Fe metal foil. Raman spectra were collected at room temperature with a Horiba Jobin-Yvon LabRAM HR spectrometer equipped with an Olympus microscope BXFM. A HeNe-laser with a wavelength of 633 nm was used as an excitation source. The spectra were collected from single granule particles by scanning surface areas of 4 × 4 μm in a range from 100 cm^{-1} to 750 cm^{-1}. The crystal structures of the synthesized materials were investigated by means of powder X-ray diffraction (PXRD). The measurements were carried out on an advanced laboratory diffractometer (Huber 5021) equipped with a microfocus rotating anode X-ray generator (Rigaku MM-007, Mo-K_α radiation, parallel collimated beam, $\varnothing \approx 2$ mm) and a 2D Pilatus 300K-W detector, with a sample to specimen distance of 0.7 m. Measurements were carried out in an angular range of $6° < 2\theta < 52°$. In order to reliably track small changes in the lattice parameter, up to ten samples were packed and separated from each other, into a single glass capillary with a diameter of 0.5 mm. Subsequently, serial measurements were carried out by translating the capillary position along the capillary rotation axis. The setup is optimized to track small changes within a series of crystalline materials while excluding common sources of error, such as sample displacement or temperature fluctuations. A detailed description of the setup is presented in ref. 33. With the diffraction patterns obtained, the crystal structures were refined by the Rietveld method[34] using the TOPAS 6 software. The estimated standard deviations were corrected according to Bérar.[35] For electrochemical characterization, 0.2 to 0.25 g of the LNMFTO materials was carefully ground by hand in order to separate agglomerated granules from each other. Preliminary slurries were prepared by mixing the additives carbon black and polyvinylidene fluoride (PVDF) with 1-methyl-2-pyrrolidinone (NMP) with a dissolver stirrer. Hereafter, the LNMFTO active materials were added and the final slurries were obtained by mixing the components with a SpeedMixer DAC 150 (Hausschild) for at least 5 minutes at 2000 rpm. Detailed information on the additives is listed in Table S2.† In the next step, the slurries were coated on Al foil with a 200 μm notch bar spreader and dried in air at 80 °C for at least 30 minutes before being transferred to a 110 °C vacuum chamber, where the drying process was continued for at least 16 hours. With final cathode compositions of 80/10/10 for LNMFTO, carbon black and PVDF, active material loadings of between 3.8 mg cm^{-2} and 4.6 mg cm^{-2} were obtained. Before cell assembly, cathodes of 12 mm in diameter were compressed by a hydraulic press with a force of 6 kN and once again dried for at least one hour in a vacuum oven at 110 °C. CR2032 coin cells were then assembled in an argon filled glovebox with lithium foil as the anode using a Whatman GF/C separator and LP30 electrolyte (1.0 M $LiPF_6$ solution in 1 : 1 v/v ethylene carbonate : dimethyl carbonate). Electrochemical measurements were carried out on a BT2000 battery cycler (Arbin Instruments) by galvanostatic charge/discharge

cycling in the voltage range of 3.5 V to 5 V. Two formation cycles at 0.1C were executed initially, followed by 10 cycles at C/2 (charging and discharging). While maintaining the charge rate of C/2, the discharge capacities at 1C and 2C were investigated (4 cycles). After two additional discharge cycles with C/2, testing of rate stability was continued by each 4 cycles with discharge rates of 5C and 10C. Hereafter, charge/discharge cycles were performed at C/2 up to a total number of 100 cycles. As a proof of principle, that this active material is suitable for industry standard battery formats and applications, an additional cathode with an active material loading of 11.6 mg cm^{-2} (corresponding to 1.65 mA h cm^{-2}) was manufactured. While the processing remained the same, the composition was changed to 90/3/3/4 wt% of LNMFTO (A2), carbon black, graphite and PVDF. A coin cell was built and cycled as described above. However, instead of Li foil, an anode made of 96 wt% graphite, 1.5 wt% carbon black and 1.25/1.25 wt% binder (Na–CMC/SRB, for details see Table S2†) with a specific capacity of about 2.5 mA h cm^{-2} was used. The cell test was extended to a total of 530 cycles, while the voltage range was reduced to 3.5 V to 4.8 V.

3. Results

3.1. Particle morphology

The SEM images of the LNMFTO materials are depicted in Fig. 1 and S3.† The results of the surface area analysis and particle size distributions are summarized in Table S1 and Fig. S1.† The spherical granules of material A1, which are obtained from the spray drying process, have diameters between 5.5 μm (D_{10}) and 13.1 μm (D_{90}) with an average value of 10.3 μm. Each sphere consists of primary particles of approximately 10 to 400 nm (*cf.* Fig. 1a–c). Additional calcination at 900 °C for 20 hours and annealing at 600 °C for 30 hours yields the starting material A2. While the particle size distribution does not change significantly during the temperature treatment (D_{10} = 6.3 μm, D_{90} = 14.3 μm and $D_{Ø}$ = 10.1 μm, *cf.* Fig. S1†), the primary particle size increases significantly. Edge lengths of larger particles are in the range of approximately 2 μm to 3 μm, while the bulk consists of smaller particles with sizes of about 0.5 μm to 2 μm (*cf.* Fig. 1d–f and S3†). The individual LNMFTO particles mostly exhibit an octahedral shape with {111} facets. Only a very few particles show a truncated octahedral shape with the extra {100} crystal facets.

During the final calcination step applied to obtain materials FC460 to FC940 and SC460 to SC940 from the starting material A2, the morphology, particle size distribution and specific surface do not change significantly anymore. As described above, this is a prerequisite for studying the specific influence of the composition and cation order. SEM images of the materials FC460 to FC940 and SC460 to SC940 hence are perfectly comparable to those shown in Fig. 1d–f. A representative selection of SEM images is provided in the ESI in Fig. S3.† The results of the specific surface analysis of the pristine material A2 and samples FC460 to FC940 are listed in Table S1.† The starting material A2 has a specific surface of S_{BET} = 0.82 m^2 g^{-1}. This value stays almost constant independent of the following heat treatments. The measurement results vary only between 0.74 m^2 g^{-1} and 0.84 m^2 g^{-1} for all samples and a combined error of measurement and evaluation[5] of ≈0.05 m^2 g^{-1} is well conceivable. Cross sections of the cathodes prepared with the starting material A2 (compositions 80/10/10 and 90/3/3/4) are depicted in Fig. 2. It is evident that the granules keep their spherical shape and inner porosity even after the densification process. From mercury intrusion porosimetry, the inner pore volume of the granules is estimated to be 20%. Details are given in the ESI in Fig. S2.†

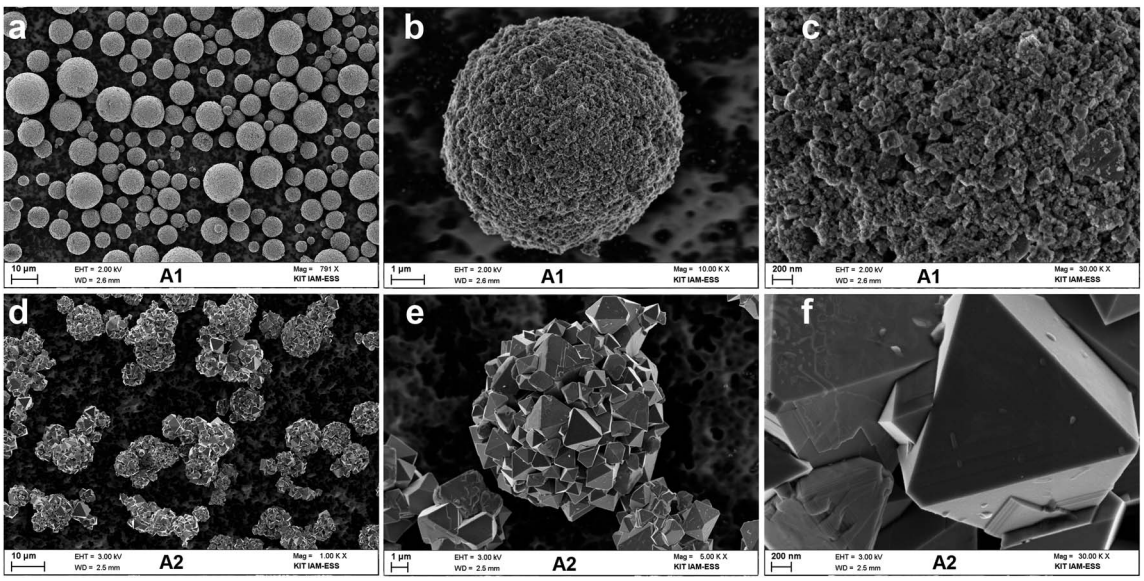

Fig. 1 SEM images of the LNMFTO granules. The material A1 as received from the spray drying process is shown in subfigures (a–c). After heat treatment for 20 h at 900 °C and 30 h at 600 °C, the starting material A2 for the final calcination processes is received (subfigures (d–f)).

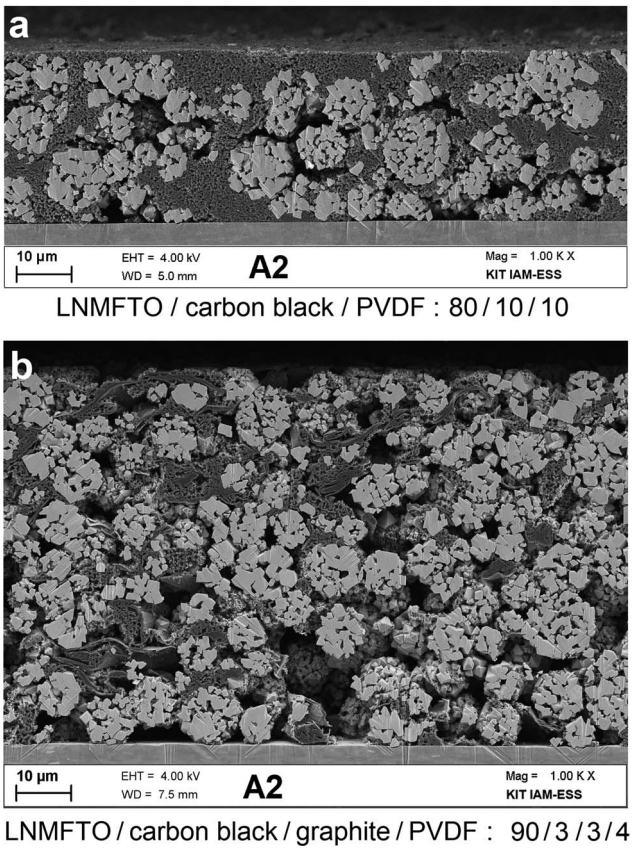

Fig. 2 Cross-sections of cathodes prepared with material A2 with compositions of 80/10/10 wt% cycled against Li (a) and 90/3/3/4 wt% cycled against graphite (b). The cathodes were compacted by using a hydraulic press. The aluminum current collectors are visible at the bottom part of the pictures.

3.2. Mößbauer spectroscopy

The Fe Mößbauer spectrum of sample A2 is shown in Fig. S4.† It consists of a doublet with isomer shift IS = 0.34 mm s^{-1} and quadrupole splitting QS = 0.77 mm s^{-1}. These values show that exclusively trivalent Fe is present, in a high-spin state, on the octahedral sites of the spinel structure.[36] Very similar values have been observed for $LiNi_{0.5}Mn_{1.5}O_4$ samples doped with 0.2–0.4 Fe.[37,38]

3.3. Raman spectroscopy

LNMO crystallizes as an ordered or disordered phase in the space groups $P4_332$ or $Fd\bar{3}m$,[4,10] or in partially ordered stages.[5,18,39] Raman spectroscopy is a comparatively simple and sensitive method to determine the structure variation at atomic levels and the short range environment of transition metal cations in LNMO spinels[40] and therefore to determine the predominant space group symmetry of LNMO samples. For undoped LNMO samples it is widely accepted that a certain extent of disorder is beneficial for electrochemical properties such as rate capability and cyclability.[13,41] The Raman spectra collected for samples SC460–SC940 and FC460–FC940 are shown in Fig. 3. In addition, the Raman spectra of sample A2 and of an undoped, ordered LNMO spinel (LNMO700) are also included. The latter material was prepared by the same spray drying technique with a final calcination of 12 h at 700 °C. All spectra were recorded with the identical measurement parameters.

The spectrum of LNMO700 matches that reported for highly ordered spinel phases (space group $P4_332$), while the spectra of the fast cooled LNMFTO samples calcined at temperatures of 700 °C and above (FC700–940) perfectly match the expectation for vastly disordered spinel samples (space group $Fd\bar{3}m$).[42] The spectra of the pristine material A2 and LNMFTO samples calcined at temperatures between 460 °C and 660 °C show properties of both ordered and disordered phases: T_{2g} and E_g modes at 160 cm^{-1} and 410 cm^{-1} exhibit higher intensities and A_{1g} modes of Mn^{4+} and Ni^{2+} at 590 cm^{-1} and 610 cm^{-1} can be distinguished, which indicates the formation of partial cation order on a local scale (Raman mode assignment according to ref. 40). Compared to the ordered LNMO, LNMFTO Raman modes are generally broadened and exhibit significantly lower intensities. This indicates that long-range order of the main transition elements manganese and nickel is effectively suppressed by the doping elements iron and titanium. The Raman spectra for the fast and slowly cooled LNMFTO samples are very similar for each temperature. This is an indication, that the formation of cation order is a rather slow process. The Raman spectra of all samples calcined between 460 °C and 540 °C hardly deviate from the spectrum of the pristine material A2, which suggests that there is almost no change in cation order at temperatures up to 540 °C. In contrast, the spectra of the samples calcined at higher temperatures between 580 °C and 660 °C show increasing intensities and more pronounced modes, which are supposed to result from an increase in cation order in that temperature range. The highest degree of cation order deduced from the spectra of FC660 and SC660 results from a total of 42 h at 600 °C and 660 °C. For temperatures higher than 700 °C up to 940 °C, Raman modes are rather weak, indicating a loss of prior cation order. The T_{2g} mode at 160 cm^{-1} and A_{1g} modes (Ni^{2+}, Mn^{3+}) at 640 cm^{-1} are slightly more pronounced for the slowly cooled samples, indicating only a gradual increase in cation order during the slow cooling process.

3.4. Powder X-ray diffraction

The PXRD diffraction pattern of the starting material A2 together with the corresponding Rietveld refinement results are shown in Fig. 4. The other 26 patterns and refinement results of the FC and SC series can be found in Fig. S6 and Table S3.† A graphical representation of the Rietveld refinement results is shown in Fig. 5a and b. The LNMFTO phases were refined using a structure model of a fully disordered spinel based on the $MgAl_2O_4$ structure-type (space group $Fd\bar{3}m$), with Ni, Mn, Fe, and Ti statistically occupying the Wyckoff site 16*c*. Superstructure reflections that theoretically arise from cation ordering and lead to a space group symmetry reduction to $P4_332$, are not visible in any of the patterns. A single isotropic displacement parameter was used for all Wyckoff sites. Refinement of the site

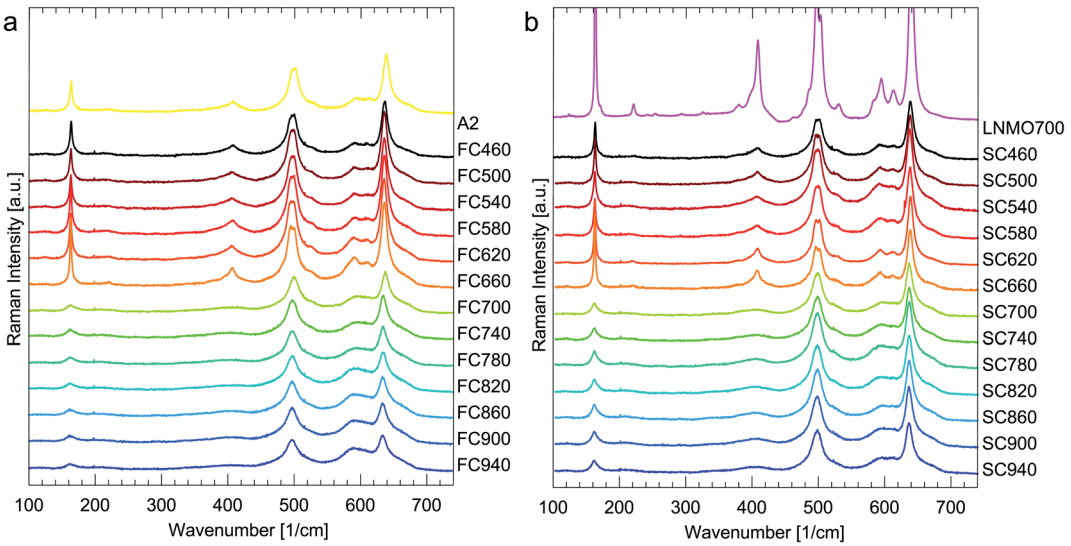

Fig. 3 Raman spectra of fast cooled (a) and slowly cooled LNMFTO samples (b). For comparison, spectra of the pristine material A2 and an ordered LNMO sample ($T_{calc.}$ = 700 °C, 12 h) are also shown in yellow and magenta. All spectra were acquired with identical measurement parameters.

occupation factor (s.o.f.) of oxygen (32*e*) yielded values of 0.980(4) to 0.988(4), corresponding to 3.92(2) to 3.95(2) oxygen anions per formula unit. The individual values are shown in Fig. 8c and listed in Table S3.† The X-ray diffraction patterns do not show any increase in the intensities of the 220 and 422 reflections at $2\theta \approx 14°$ and 30.5°, respectively (*cf.* Fig. 4a and S6†), which indicates that the 8a Wyckoff site (tetrahedral voids) is occupied by lithium exclusively.[26,27,29,43]

While the lattice parameters of LNMFTO spinel could be refined very accurately, the phase fraction of the secondary phase, mostly referred to as the rocksalt phase in the literature, is rather difficult to determine reliably. As highlighted in Fig. 4b–d, major reflections of both phases overlap, which makes it difficult to refine profile parameters independently. Furthermore, the composition of the secondary phase is not known exactly, resulting in the problem that the phase fractions of the main and secondary phases are highly correlated to the Li/Ni ratio of the secondary phase. Moreover, this secondary phase is mostly described as, *e.g.* $Li_xNi_{1-x}O$,[44] $(Li_xMn_{0.66}Ni_{0.34})_yO$ [4] or $(Li_{0.33}Mn_{0.5}Ni_{0.167})_xO$ [11] (space group $Fm\bar{3}m$, $a \approx$ 415 pm). However, upon a closer inspection of the diffraction patterns additional reflections at $2\theta \approx 8.5°$ are found, which ought to be extinct for a cubic phase. In accordance with the elemental distribution found in SEM-EDX analysis (*cf.* Fig. S5†), the secondary phase was refined as $Li_xNi_{1-x}O$ by applying a model of the α-$NaFeO_2$ structure type (space group $R\bar{3}m$, $a \approx$ 293 pm, $c \approx$ 1440 pm, and x = 0.33). The corresponding compounds with suitable lattice parameters have been described for Li-rich $Li_xNi_{1-x}O$ samples ($x > 0.28$)[45] and iron containing oxides such as. $Li_{0.45}(Ni_{0.40}\ Fe_{0.1})_{1.14}O$,[46,47] both of which seem plausible on the basis of the high iron content of LNMFTO.

The lattice parameters of LNMFTO in the FC and SC series range from 818.22 pm to 819.64 pm. The minimum is found for sample SC660 ($T_{calc.}$ = 660 °C) and the maximum for FC940 ($T_{calc.}$ = 940 °C). Refinement of samples calcined at 460 °C up to

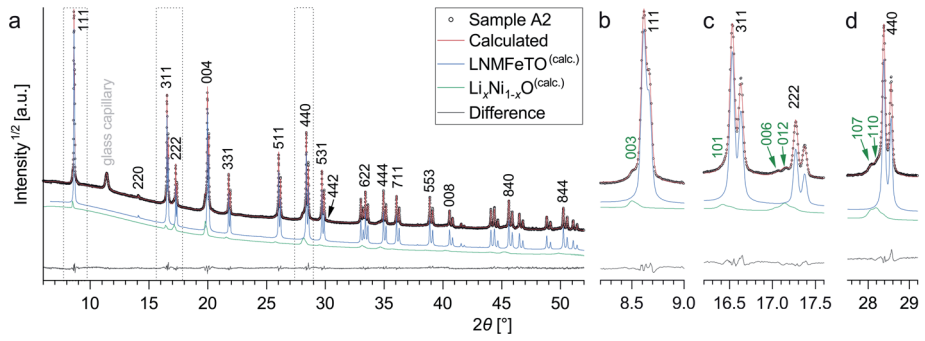

Fig. 4 (a) Rietveld refinement of the starting material A2 with the individual contributions of the LNMFTO (blue) and $Li_xNi_{1-x}O$ phase (green). For visualization purposes, the contributions of the individual phases were set off vertically. Reflection indices of LNMFTO and $Li_xNi_{1-x}O$ are labelled in black and green. The enlarged 2θ ranges in subfigures (b–d) show the reflection overlap and individual contributions of the main and secondary phases. Double reflections result from Mo-$K_{\alpha 1,2}$ splitting. The square root of the intensity was chosen to emphasize weak reflections.

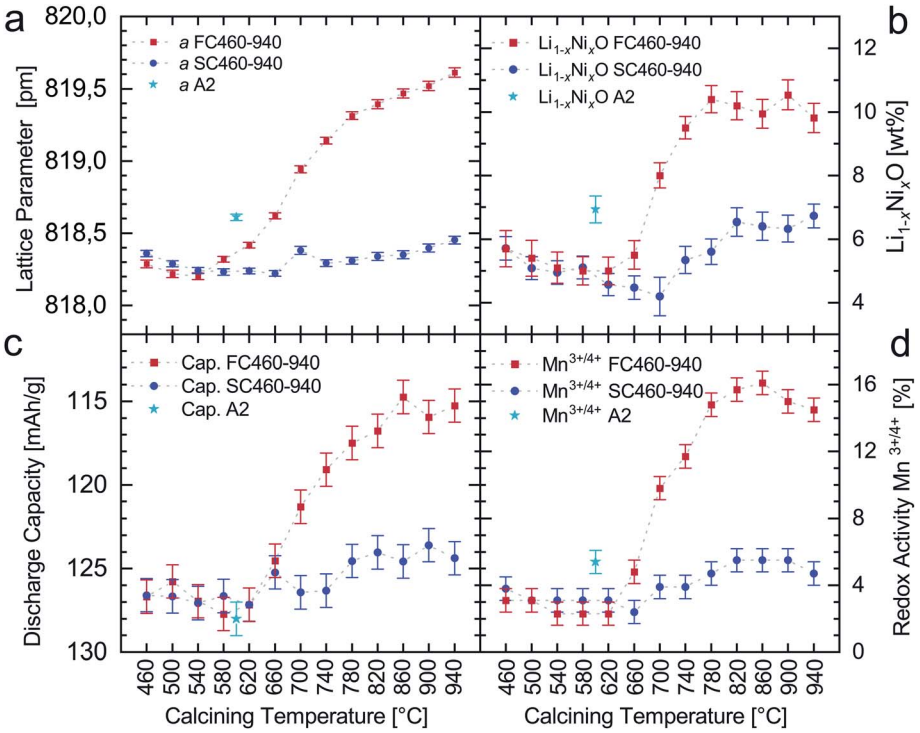

Fig. 5 Results of the Rietveld refinement (a and b) in comparison to the results of cell tests (c and d). Discharge capacities correspond to the 3rd cycle (1C). An error of 1 mA h g^{-1} is assumed due to coin cell making and measurement. The discharge capacity axis is inverted to highlight the correlation with the lattice parameter. The data acquisition for subfigure (d) is described in Fig. S7.† Dashed lines are a guide for the eye.

620 °C generally yields smaller lattice parameters compared to the starting material A2 (a = 818.58(2) pm), indicating that the remaining Mn(III) ions of the starting material A2 are further oxidized to Mn(IV) during these thermal treatments.

Fig. 5a shows that calcination at temperatures of 580 °C and above, followed by a fast cooling rate, leads to an increase in the lattice parameters (samples FC580 to FC940), which is commonly attributed to the loss of oxygen and reduction of Mn^{4+} to Mn^{3+} (ionic radii: Mn^{IV}: 53 pm; Mn^{III}: 64.5 pm (ref. 16)). The corresponding slowly cooled samples SC580 to SC940 undoubtedly show very similar lattice parameters at the end of the high temperature stage in the calcination process. However, the slow cooling rate within the temperature range of 650 to 450 °C (10 K h^{-1}) allows for the reversal of the lattice parameter extension by a large extent due to the re-oxidation of Mn^{3+} to Mn^{4+}. This redox activity is confirmed by the evaluation of the voltage profiles (shown in the section Electrochemistry).

The samples calcined at 460 and 500 °C show slightly increased lattice parameters compared to those calcined at 540 °C, which is presumably for kinetic reasons: the oxidation of the remaining Mn(III) ions might be slow at these low calcination temperatures and, as a consequence, thermodynamic equilibrium cannot be reached within the calcination time. The fast cooled samples reveal a minimum of the lattice parameter at 540 °C (FC540, a = 818.23(3) pm), which is within the error range of the absolute minimum of SC660 (a = 818.22(2) pm). The increased lattice parameters of the samples FC580 and FC620 suggest that the onset of secondary phase formation, linked to oxygen release and reduction of Mn(IV), should be found within this temperature range between 540 °C and 580 °C. In contrast, oxygen release for undoped LNMO has been reported to start from 620 °C to 650 °C [11] or 690 °C.[5]

The phase fractions of the secondary phase were refined from 4.2 wt% (SC700) to 11.0 wt% (FC940). For the starting material, a secondary phase fraction of 6.9 wt% was found. However, it is possible that newly formed domains of the secondary phase are amorphous or nanocrystalline and therefore cannot be recognized in the diffraction patterns. Thus, the real phase fractions can vary somewhat. Some basic findings can nevertheless be pointed out. Firstly, it is difficult to obtain a Fe–Ti doped LNMO-material with phase fractions of the secondary phase below 4 wt%, when calcining under the ambient atmosphere. Secondly, when calcining at 700 °C and above, the formation of an additional secondary phase is accelerated drastically. Finally, from Fig. 5b it becomes obvious that the secondary phase newly formed in the temperature range of 700 °C to 940 °C almost fully, and thus quickly, transforms back to LNMFTO during cooling with a slow cooling rate.

3.5. Electrochemistry

The results of the battery testing for the pristine material A2, and the materials FC460 to FC940 and SC460 to SC940 are depicted in Fig. 6. The discharge capacities of the third cycle (after formation; hereafter referred to as "starting capacity") and the contributions of the $Mn^{3+/4+}$ redox couple to the total

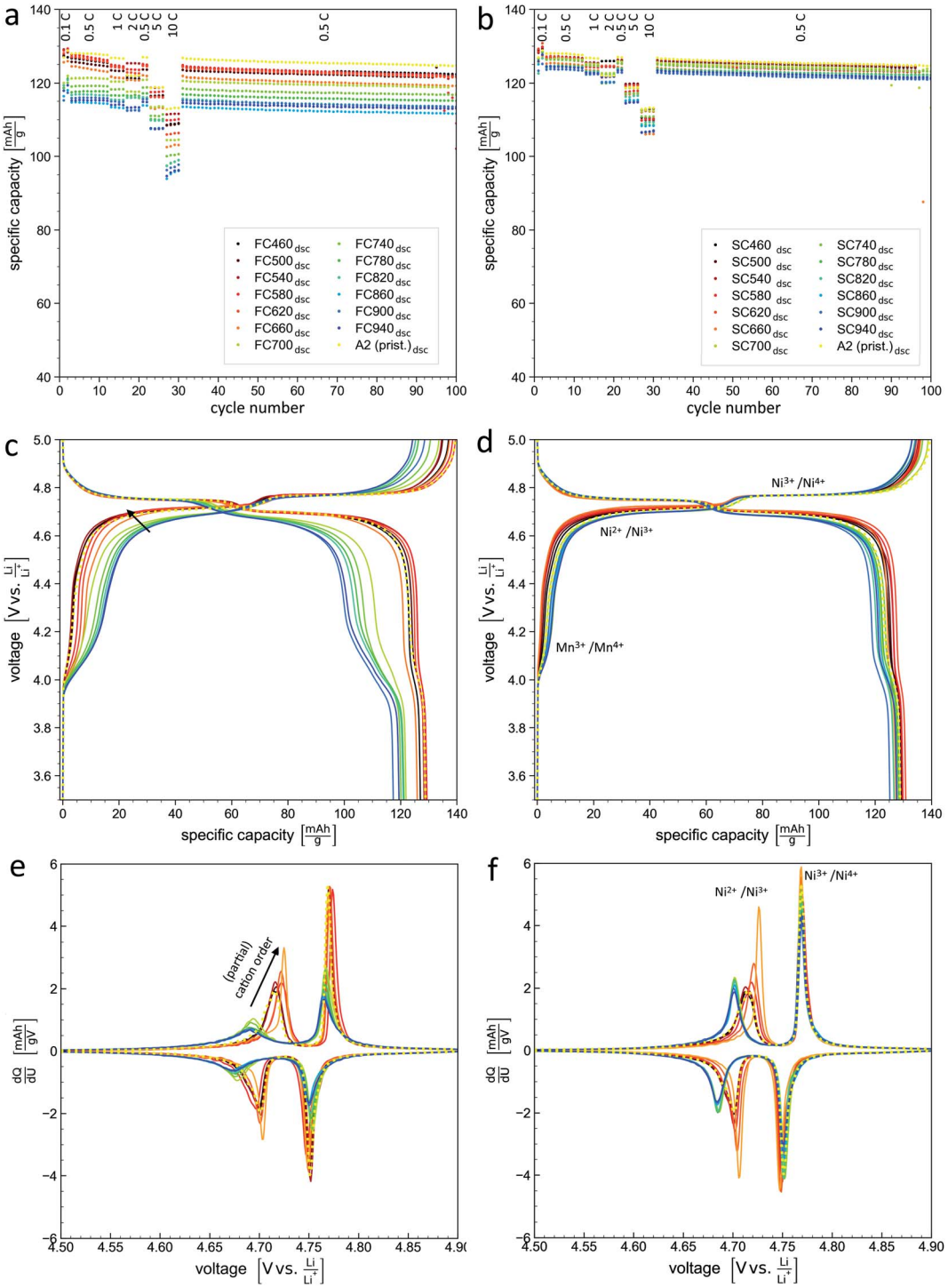

Fig. 6 Electrochemical characterization of the LNMFTO materials with fast cooled samples on the left (a, c and e) and slowly cooled samples on the right (b, d and f). The starting material A2 is plotted in yellow and highlighted by a dotted line in (c–f). Subfigures (a) and (b) show the specific discharge capacity during the first 100 cycles. The capacity *vs.* voltage profiles of the second cycle are shown in (c) and (d). The corresponding dQ/dU-profiles are depicted in (e) and (f). Samples colored black to orange indicate partial cation-order according to Raman spectroscopy, while samples colored light green to dark blue are vastly disordered.

capacity are shown separately in Fig. 5c and d. The latter were derived from the voltage profiles shown in Fig. 6c and d. The pristine material A2 has a starting capacity of 128.0 mA h g^{-1}. All slowly cooled materials and the fast cooled materials calcined between 460 °C and 660 °C show comparable capacities of 127.7 mA h g^{-1} to 124.5 mA h g^{-1}. A substantial decrease in the starting capacities is only observed for the fast cooled samples calcined between 700 °C and 940 °C (121.3 to

114.7 mA h g^{-1}). Fig. 6a and b also show that the discharge capacities for 1C and 2C hardly deviate from those observed at 0.5C and even at 5C and 10C LNMFTO shows excellent rate stability with capacities larger than 105 mA h g^{-1} and 90 mA h g^{-1}, respectively. After the formation cycles and the rate test, all samples show very similar cycling stabilities. Compared to the 30th cycle, capacity retentions of 98.1% to 98.7% are observed during the following 70 cycles, regardless of cation order and phase composition.

The voltage *vs.* capacity profiles of the charge and discharge processes of the second cycles are depicted in Fig. 6c and d. In previous studies of a Ti–Fe doped LNMO with a very similar composition,[30] the three redox plateaus were assigned to three different redox couples: Mn^{3+}/Mn^{4+} at around 4.1 V, Ni^{2+}/Ni^{3+} at around 4.7 V and Ni^{3+}/Ni^{4+} at 4.75 V. In full agreement with the Raman spectra and literature,[9,22] the gap between the two Ni-redox plateaus decreases when the cation order increases. The Ni^{2+}/Ni^{3+} redox plateau is situated at ~4.68 V for the fully disordered, and ~4.71 V for the partially ordered structure. The voltage *vs.* capacity profiles of the slowly cooled samples are very similar. The differences between the vastly disordered (colors green to blue) and partially ordered samples (colors black to orange) are hardly noticeable. The nickel related redox activity dominates the charging and discharging processes and almost exclusively contributes to the total capacity; a minor contribution is related to the $Mn^{3+/4+}$ redox couple (step at 4.1 V). Deviating profiles are found for the fast cooled samples calcined at 660 °C and above, as a gradual increase of the Mn^{3+}/Mn^{4+} step is observed, while the Ni^{2+}/Ni^{4+}-step is less pronounced and the overall capacity diminishes. From the profiles the relative content of redox active $Mn^{3+/4+}$ can be derived.[19] A corresponding evaluation of the discharge curves is shown in Fig. S7† and yields contents of 2.4 to 5.5% of electrochemically active $Mn^{3+/4+}$ in the slowly cooled samples and 2.3 to 16.1% for the fast cooled samples. The results for the individual samples are shown in Fig. 5d and Table S4.†

The dQ/dU profiles of the second cycle in the voltage region between 4.5 V and 4.9 V are shown in Fig. 6e and f. Slowly cooled samples generally show sharper peak profiles. In good agreement with the results of Raman spectroscopy, they allow for a clear distinction between the partially ordered and the fully disordered samples.[9] The latter exhibit a larger separation of the maxima and the lower level of the Ni^{2+}/Ni^{3+} redox couple is situated at a slightly lower potential. The cation order is essentially the same for the starting material A2 and all samples calcined between 460 °C and 540 °C. From 580 °C, the cation order increases with increasing calcination temperature up to 660 °C. Higher calcination conditions at 700 °C and above finally lead to a loss of cation order and the dQ/dU profiles of these samples are nearly indistinguishable.

The result of the cell test with the highly loaded cathode (material A2, 1.65 mA h cm^{-2}) cycled against a graphite anode is shown in Fig. 7. A cross section of the cathode is shown in Fig. 2b. Compared to the cell with the same active material cycled against lithium, the discharge capacity of the second cycle (0.1C) is reduced by 8.4 mA h g^{-1} to 120.4 mA h g^{-1} indicating some irreversible Li loss during the solid electrolyte interface formation. Nevertheless, in the full cell, the rate dependent capacities up to 5C are hardly reduced compared to the first 10 cycles at 0.5C. Only when the discharge capacities are increased to 10C, a significant reduction of the cell capacity to approximately 73 mA h g^{-1} was observed, which, however might also be an effect of the graphite anode. After the rate test, a capacity of 113.0 mA h g^{-1} was measured in the 30th cycle for charge/discharge rates of 0.5/0.5C. After 500 more cycles, a discharge capacity of 100.6 mA h g^{-1} was observed, corresponding to a capacity retention of 89.0%.

4. Discussion

4.1. Morphology and composition

The SEM images of the active materials and BET examinations of the specific surface show that the fast and slowly cooled samples FC460 to FC940 and SC460 to SC940 have very similar morphological properties, which was the stated goal of the calcination programs yielding these samples (*cf.* Table S1 and Fig. S3†). Consequently, particle morphology and specific surface area are very unlikely to have a significant impact on the electrochemical properties of the materials and can be neglected in the following discussion. As confirmed by the cross section of a compressed electrode, the granules are mechanically stable, which makes them suitable for industrial processing (*i.e.* calendaring). In addition, Li-diffusion pathways remain rather short due to internal porosities of about 20% (*cf.* Fig. 2 and S2†). For the applied spray-drying technique, previous studies on Fe–Ti-doped LNMO spinels showed excellent consistency between the starting materials and the composition of the final synthesized materials.[29,30] Likewise, in the present study, the experimental results for most samples are in very good agreement with the theoretical composition of $LiNi_{0.5}Mn_{1.37}Fe_{0.1}Ti_{0.03}O_{3.95}$; significant deviations presumably occur in the samples quenched at high temperatures (FC700 to FC940). Thus, for a good understanding of the electrochemical properties, it is necessary to have a detailed discussion of the compositions and the crystal structure.

The preferential occupation of the octahedral positions for titanium was reported previously in ref. 25 and is confirmed by the Rietveld refinements. Due to the higher ionic radii of Ti(IV) compared to Mn(IV) (60.5 pm *vs.* 53 pm (ref. 16)) an expansion of the unit cell is expected. In a study on $LiNi_{0.5}Mn_{1.5-x}Ti_xO_4$ ($0 < x < 1$) this expansion was found to obey Vegard's rule[25] and accordingly, for LNMFTO, with 0.03 titanium ions per formula unit (f.u.) a Ti-related lattice parameter increase of 0.38 pm is expected. The total increase in the lattice parameter of LNMFTO however, sums up to about 1.8 pm compared to undoped LNMO, where a = 816.4 pm and 816.5 pm are found for calcining temperatures of 500 °C and 600 °C, respectively.[4] Thus major parts of the increase in a have to be attributed to the iron doping. In a further study, lattice parameters of 818.56 pm and 816.93 pm were reported for $LiNi_{0.42}Mn_{1.5}Fe_{0.08}O_4$ and $LiNi_{0.5}Mn_{1.5}O_4$ annealed at 700 °C,[43] resulting in a Fe(III) related lattice parameter increase of 1.63 pm. For LNMFTO, Mößbauer spectroscopy proves that iron is present in a d^5-high-spin state, and that Fe(III) ions occupy octahedral positions exclusively. The

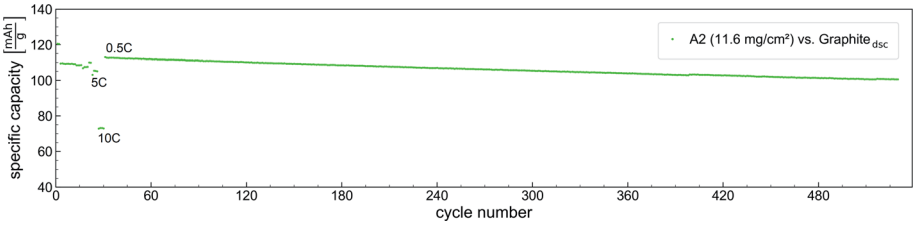

Fig. 7 Specific capacity *vs.* cycle number for material A2 cycled against graphite.

corresponding Shannon radii (64.5 pm (ref. 16)) are notably enlarged compared to those of Mn(IV), and thus, our findings are in good agreement with these previous studies and the lattice parameter increase confirms the Fe–Ti doping.

However, for the substitution of Mn(IV) by Fe(III), charge balance needs to be maintained in LNMFTO. Following the concept of oxygen nonstoichiometry, *i.e.* the underoccupation of the oxygen position in the O^{2-}-f.c.c. sublattice, one oxygen vacancy is expected per two Fe(III) ions. Thus, for 0.1 Fe(III) cations per formula unit 3.95 instead of 4 oxygen anions should be present for the oxidized and lithiated states, leading to the initially mentioned formula $LiNi_{0.5}Mn_{1.37}Fe_{0.1}Ti_{0.03}O_{3.95}$. The slightly reduced oxygen content is in good agreement with the results of the Rietveld refinement, where in average 3.94(3) oxygen anions per f.u. are found. Fe(III) charge balancing mechanisms without oxygen vacancies are hardly conceivable due to inconsistencies with the other experimental results: higher nickel oxidation states do not match the electrochemical investigations, and higher oxidation states of manganese or an excess of lithium would lead to noticeable changes in the crystal structure.

4.2. Cation order and Mn(III) content

From the comparison with Raman spectra of ordered LNMO, and in accordance with the Raman results of previous studies[28] it is evident that Ti–Fe doping effectively suppresses the formation of well-ordered crystal domains and all LNMFTO samples investigated herein can be considered completely or predominantly disordered. Raman spectra are in perfect agreement with the findings from the dQ/dU plots. It becomes obvious, that for LNMFTO, the formation of (partial) cation order, is a slow process that lasts days rather than hours. Furthermore, it is limited to a rather small temperature range, as only samples calcined at 580 °C, 620 °C and 660 °C show increasing cation order. The rather quick transition from (partially) ordered to the fully disordered state is found within the temperature range of 660 °C to 700 °C, which is reduced compared to undoped LNMO. For the latter, a predominantly ordered state is found at 700 °C and the transition to the fully disordered state was reported at about 730 °C.[5,18] Apart from the fact that the Ni^{2+}/Ni^{3+} redox plateau is situated at a slightly lower potential of about 4.68 V *vs.* 4.71 V (*vs.* Li/Li^{+}) for the partially ordered materials, there is no evidence that cation order is relevant regarding electrochemical properties such as capacity, charge and the discharge mechanism or degradation of this active material. In fact, the very similar cell degradation is a strong argument that particle shape and specific surface – which hardly deviate for the samples investigated herein – are more important factors for cell ageing, at least when cycling against lithium.

According to the expansion of the unit cell in the fast cooled series, elevated ratios of Mn(III) are observed from 580 °C on and steadily increase until 940 °C. The X-ray diffraction patterns also prove that high Mn(III) ratios formed during high temperature treatment and preserved in the fast cooled samples are almost fully compensated during slow cooling in the temperature range of 650 °C to 350 °C (10 K h^{-1}) (*cf.* Fig. 5c). This unambiguously shows that the formation and compensation of Mn(III)-ions (and the oxygen defects assigned) are much faster processes than the formation of (partial) cation order. Concerning the general discussion on LNMO materials, this also points out that the cooling rate can play a much more important role for the Mn(IV)/Mn(III) ratio than the calcination temperature.

From Fig. 5b it becomes evident, that the fast cooled samples calcined at 660 °C and below show reduced side phase fractions compared to the starting material A2, while all FC samples calcined at 700 °C and above show increased ratios. In the small temperature range of 660 °C to 700 °C the onset of accelerated secondary phase formation thus coincides with the loss of (partial) cation order discussed before. It is quite plausible that an increase in cation mobility within the spinel structure, or more precisely, between the tetrahedral and octahedral voids, is a prerequisite for both the loss of cation order and formation of the secondary phase.

Comparison of the Rietveld refinements and the cell tests shows a close correlation between the lattice parameter of LNMFTO and its discharge capacity (Fig. 8a). The lattice parameter thus can provide information on the success or failure of a calcination program and can be used as a proxy variable for the capacity at a very early stage of the battery manufacturing process. Presumably as a side effect of the Fe–Ti doping, the secondary phase observed in this study most likely has trigonal symmetry and thus is not a "rocksalt" phase. The actual composition could not be determined beyond any doubt in the course of the work. However, the correlation between the redox activity of $Mn^{3+/4+}$ and the phase fraction of the side phase shown in Fig. 8b supports the assumption that this phase is rather Ni-rich. The SEM-EDX mapping shown in Fig. S5† also indicates that the phase has a significantly higher Ni-content, while the amount of Mn is reduced compared to the main phase. Based on the EDX images, it is furthermore conceivable

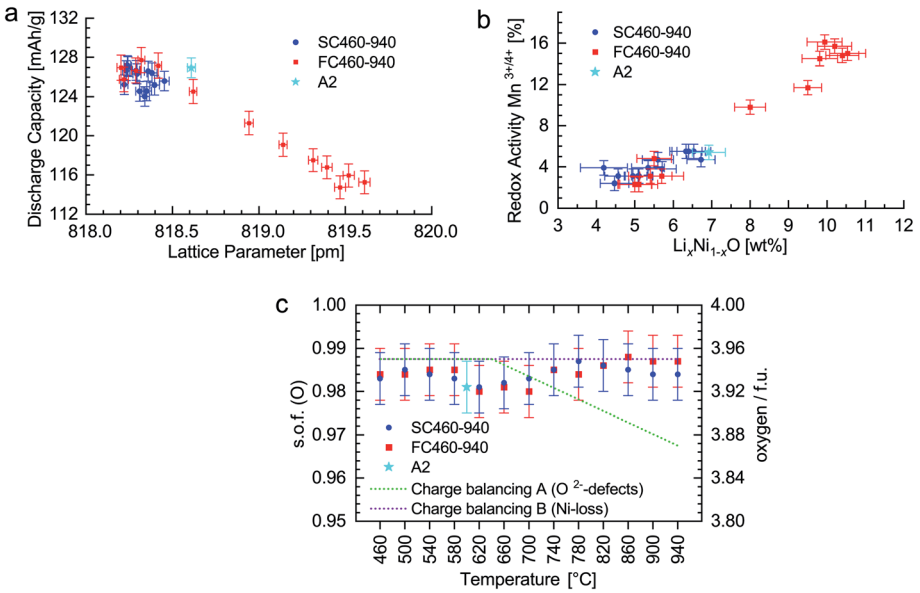

Fig. 8 Correlations between the discharge capacity and the lattice parameter (a) and between the redox activity of $Mn^{3+/4+}$ and the phase fraction of the $Li_{1-x}Ni_xO$-phase (b). Subfigure (c) shows the oxygen site occupancy factor (s.o.f.) and corresponding amount of oxygen per formula unit obtained by the Rietveld refinement. The purple dots represent the theoretical value of 0.9875 for any composition $LiNi_{0.5-y}Mn_{1.37+y}Fe_{0.1}Ti_{0.03}O_{3.95}$ (charge balancing mechanism B), while the green line represents the expected values for oxygen defects forming at 650 °C and above with compositions $LiNi_{0.5}Mn_{1.37}Fe_{0.1}Ti_{0.03}O_{3.95-\delta}$ ($0.01 < \delta < 0.08$).

that the secondary phase contains iron, but it is very unlikely that it is iron-rich in particular.

The amount of the secondary phase and the ratio of redox active manganese increase significantly between 660 °C and 700 °C. According to the proposed charge balancing mechanisms, two explanations are conceivable: corresponding to the mechanism A, for two Mn(III) ions, one additional oxygen defect is expected, which leads to the formal composition $LiNi^{II}_{0.5}Mn^{IV}_{1.37-2\delta}Mn^{III}_{2\delta}Fe^{III}_{0.1}Ti^{IV}_{0.03}O^{-II}_{3.95-\delta}$. According to the discharge profiles of the individual materials, 2% to 16% of the overall capacity results from Mn^{3+}/Mn^{4+} redox activity, corresponding to the δ values of 0.01 to 0.08 and overall compositions of $LiNi_{0.5}Mn_{1.37}Fe_{0.1}Ti_{0.03}O_{3.94}$ to $LiNi_{0.5}Mn_{1.37}Fe_{0.1}Ti_{0.03}O_{3.87}$. Such δ values are in good agreement with those discussed in the literature,[11] however, they are not reflected in the site occupancy factors of oxygen refined from the PXRD patterns (Fig. 8c). At least for the FC samples, the oxygen content should roughly correspond to the green line, which is obviously not the case. When assuming a rather Ni-rich secondary phase, a Ni-depletion of the LNMFTO phase is expected. According to the balancing mechanism B suggested by the Cabana group,[4,9,17] a composition $LiNi^{II}_{0.5-y}Mn^{IV}_{1.37-y}Mn^{III}_{2y}Fe_{0.1}Ti_{0.03}O_{3.95}$ would result in y values of 0.01 to 0.08 for 2% to 16% Mn(III), corresponding to the compositions $LiNi_{0.49}Mn_{1.38}Fe_{0.1}Ti_{0.03}O_{3.95}$ to $LiNi_{0.42}Mn_{1.45}Fe_{0.1}Ti_{0.03}O_{3.95}$, which is in good agreement with the s.o.f. of oxygen and the correlation shown in Fig. 8b.

A decisive detail supporting the second hypothesis (Ni-depletion, balancing mechanism B) is that in the voltage profiles of the Mn(III) rich samples FC700 to FC940 the redox plateaus of Ni^{2+}/Ni^{3+} are equally or less pronounced compared to the Ni^{3+}/Ni^{4+} plateaus (see Fig. 6c and S7†). The corresponding redox contributions are listed in Table S4† and indicate that all nickel present in the structures is oxidized to Ni(IV) during charging. If, according to the balancing mechanism A, oxygen vacancy formation was the reason for the presence of Mn(III) in LNMFTO and, according to $LiNi_{0.5}Mn_{1.37}Fe_{0.1}Ti_{0.03}O_{3.95-\delta}$, 0.5 Ni ions per formula unit were still available in the materials, one would inevitably expect significant amounts of Ni(III) not to be fully oxidized to Ni(IV) during charging. Thus the Ni^{3+}/Ni^{4+} plateaus would have to be less pronounced in the voltage profiles, which is not the case.

This argument likewise applies to LNMO and is illustrated in detail for a material with $\delta = 0.1$ and the hypothetical composition $LiNi_{0.5}Mn_{1.5}O_{3.9}$ ($=LiNi^{II}_{0.5}Mn^{IV}_{1.3}Mn^{III}_{0.2}O_{3.9}$): During charging, in the first step, Mn(III) is oxidized to Mn(IV) coming along with a loss of 0.2 lithium and leading to the composition $Li_{0.8}Ni^{II}_{0.5}Mn^{IV}_{1.5}O_{3.9}$. Subsequently, at an increased potential, Ni(II) is oxidized to Ni(III) and 0.5 lithium is extracted, yielding $Li_{0.3}Ni^{III}_{0.5}Mn^{IV}_{1.5}O_{3.9}$. Finally, by extracting the remaining lithium, only 60% of the Ni(III) is oxidized to Ni(IV) in the fully delithiated state $Ni^{IV}_{0.3}Ni^{III}_{0.2}Mn^{IV}_{1.5}O_{3.9}$, and thus, the Ni^{3+}/Ni^{4+} redox plateau ought to be narrower, which to the best of our knowledge has never been observed so far. When, in contrast, Ni-depletion according to $LiNi^{II}_{0.4}Mn^{IV}_{1.4}Mn^{III}_{0.2}O_4$ is the reason for the occurrence of Mn(III) in LNMO, redox activity is expected to be split into 20%, 40% and 40% for Mn^{2+}/Mn^{3+}, Ni^{2+}/Ni^{3+} and Ni^{3+}/Ni^{4+}.

Finally our results show that both concepts A (oxygen defects) and B (transition metal off-stoichiometry) are necessary to explain particular experimental findings of LNMFTO. Iron doping cannot be explained without oxygen defects, while, the properties of the fast cooled samples calcined at temperatures of 700 °C and above

have to result from variations of the Ni/Mn ratio. Hence, we consider that both have their areas of validity, do not exclude each other and can coexist in LNMO-materials. With $0.01 \lesssim y \lesssim 0.03$ for $LiNi_{0.5-y}Mn_{1.37+y}Fe_{0.1}Ti_{0.03}O_{3.95}$, A2, all slow cooled samples and the fast cooled samples calcined up to 660 °C are close to the ideal LNMFTO composition ($y = 0$). For FC700 to FC940, y was calculated to be 0.05–0.08. The values for the individual samples are found in Table S4.† Some minor observations cannot be reconciled with the aforementioned concepts and the previous assumptions on the electrochemical and crystallographic properties of LNMFTO: according to the slightly increasing lattice parameter of the fast cooled samples FC540 to FC660, increasing contents of Mn(III) are expected in the temperature range between 540 °C and 620 °C, while the corresponding voltage profiles in contrast suggest a decline of Mn(III) in the same samples. The divergence is rather small but as we do not suspect a measurement error, this might indicate that additional peculiarities have to be taken into account to fully understand LNMFTO. However, unless better data is available, no solid conclusions can be drawn on this specific point.

4.3. Electrochemistry

According to the common notions of LNMO degradation mechanisms, Mn(III) dissolution is a crucial factor for cell ageing and capacity fade, especially when cycled against graphite.[2,48] Therefore, the Mn(III) content was minimized in the starting material A2. When cycled against lithium, all LNMFTO materials show very similar degradation behavior and no systematic trends are discernible. Thus, we conclude that morphological properties and cell preparation are the most significant parameters regarding cell degradation when cycled *vs.* lithium. Deviations in the composition and crystal structure play only a minor role. Based on the composition $LiNi_{0.5}Mn_{1.37}Fe_{0.1}Ti_{0.03}O_{3.95}$, the specific capacity for LNMFTO is 147.4 mA h g^{-1} which is very close to the theoretical capacity of LNMO (146.7 mA h g^{-1}). However, in the cell tests, capacities of only 131 mA h g^{-1} were found when charging and discharging at 0.1C. This, on one hand, is slightly increased compared to previous results for LNMFTO,[29] but on the other hand is still significantly reduced compared to undoped LNMO materials, where capacities above 140 mA h g^{-1} are reached.[49] This capacity reduction is mainly due to rather large primary particles and the high amount of the secondary phase. It was not possible to minimize the phase fraction below 4 wt% which should be a goal for further optimization of the synthesis procedure. However, the decisive advantages of LNMFTO are good rate capability, excellent cycle stabilities and transferability to full cells. The results of our preliminary test, in which the starting material A2 was cycled against a graphite anode, are to the best of our knowledge superior to all previous results for LNMO/graphite cells that are vaguely heading towards industrial relevance (a detailed discussion and literature review on LNMO full cells is found in ref. 49). As shown in Fig. 7, for a thick LNMFTO cathode (11.6 mg cm^{-2}) cycled against graphite, a capacity of over 105 mA h g^{-1} at discharge rates of 5C and capacity retention of >89% over 500 cycles are obtained.

4.4. Calcination

For LNMO, it is reported that the onset of oxygen release and the order–disorder transition temperature depend on oxygen partial pressure,[5,15] and thus for LNMFTO these transition temperatures can most likely be modified by calcining in more oxygen-rich environments. The LNMFTO calcination experiments show that desired morphological properties, such as crystal size and shape as well as granule porosity can be adjusted in the first step by appropriate calcination temperatures and dwell times. Afterwards, chemical and crystallographic properties such as the cation order and Mn(III) content (with the related transition-metal off-stoichiometry) can be modified independently from each other and independently from the morphological properties at rather low calcination temperatures below 700 °C. To minimize unwanted secondary phase fractions and to oxidize Mn(III) to Mn(IV), slow cooling rates or dwell times at temperatures lower than 660 °C are advisable. If the formation of cation order is undesired, temperatures of 460 °C to 540 °C can be chosen. If (partial) cation order is already present in a given sample, a short increase in the temperature up to 700 °C should suffice to yield a mainly disordered crystal structure. Taking into account the deviating transition temperatures from the ordered to the disordered state and the deviating onset of Mn(III) formation (or oxygen release, respectively), we assume that our two step calcination approach is transferable to undoped LNMO.

5. Conclusion

A high-voltage LNMO spinel with Fe–Ti doping (LNMFTO) was synthesized in a two-step spray drying approach. The basic idea for materials design to minimize cathode related cell degradation was to minimize the specific surface while separately maintaining sufficient porosity to facilitate lithium diffusion. Therefore, a starting material (A2) with a specific surface of ~0.7 m^2 g^{-1}, primary particle size of 0.5 μm to 3 μm and an inner pore volume of 20% was prepared by calcining at 900 °C for 20 h. In order to restore the capacity losses related to the formation of the secondary phase and to reduce the Mn(III) content, a 20 h dwell time at 600 °C was added. Subsequently, for a detailed understanding of the influence of thermal treatment on the crystal structure and electrochemical performance, additional thermal treatments at 460 °C to 940 °C in steps of 40 °C, combined with fast and slow cooling rates were applied. Dwell times were selected in a way that allowed the crystal structure and chemical composition to change, while the aforementioned morphological properties remained essentially the same.

In a combined investigation by means of PXRD, Raman spectroscopy and cell tests, the correlations between crystallographic and electrochemical properties were examined and discussed in detail. LNMFTO has an ideal composition of $LiNi^{II}_{0.5}Mn^{IV}_{1.37}Fe^{III}_{0.1}Ti^{IV}_{0.03}O_{3.95}$. The doping elements are electrochemically inactive within the voltage window of 3.5 to 5 V and suppress the formation of large scale cation order. Instead, partially ordered or fully disordered states were found, which

hardly affect the electrochemical properties. It is clearly confirmed that (partial) cation order and the reduction of Mn(IV) to Mn(III) associated with the loss of oxygen are independent phenomena emerging and vanishing at different temperature and time scales. Our findings suggest that the onset of secondary phase formation coincides with the loss of partial cation order and thus suggest that these phenomena might be related.

At high temperatures, the formation of a trigonal secondary phase is observed accompanied by a loss of nickel in the active material, leading to increased Mn^{3+}/Mn^{4+} redox activity and capacity loss which are reversible to a large extent due to slow cooling. Experimental findings clearly contradict the formation of oxygen defects in the spinel phase during high temperature treatment. Slowly cooled samples exhibit the highest capacity and energy density, and redox activity is almost exclusively attributed to Ni^{2+}/Ni^{4+} (4.7 V *vs.* Li/Li^+). Thus, these materials are best suited for application in full cells. A preliminary test shows that LNMFTO is a competitive material for high-power and high-energy applications, as capacity fade is reduced compared to all previously reported LNMO materials with high areal capacity.

Author contributions

Pirmin Stüble performed conceptualization, methodology, lead investigation, writing – original draft, writing – reviewing and editing and project administration. Joachim R. Binder acquired the funding, Holger Geßwein carried out the supervision. Both performed writing – review & editing. Sylvio Indris carried out supporting investigation and writing – review & editing. Marcus Müller, Daniela Linder, Margarete Offermann, Nicole Bohn, Alexander Vogt and Valeriu Mereacre contributed by supporting the investigation.

Conflicts of interest

The authors declare no conflict of interest.

Acknowledgements

We would like to thank Nicole Bohn, Daniela Linder, Margarete Offermann and Alexander Vogt for their support on material synthesis, surface area and size distribution analysis and mercury intrusion porosimetry. We also thank Valeriu Mereacre for the valuable discussions and preparative work for Mößbauer spectroscopy and Nicola R. Kroll for proofreading. The work contributes to the research performed at CELEST (Center for Electrochemical Energy Storage Ulm-Karlsruhe).

References

1 J. Chen, Z. Huang, W. Zeng, F. Cao, J. Ma, W. Tian and S. Mu, Synthesis, Modification, and Lithium-Storage Properties of Spinel $LiNi_{0.5}Mn_{1.5}O_4$, *ChemElectroChem*, 2021, **8**, 608–624.

2 J.-H. Kim, N. P. Pieczonka, Z. Li, Y. Wu, S. Harris and B. R. Powell, Understanding the capacity fading mechanism in $LiNi_{0.5}Mn_{1.5}O_4$/graphite Li-ion batteries, *Electrochim. Acta*, 2013, **90**, 556–562.

3 J.-H. Kim, N. P. W. Pieczonka and L. Yang, Challenges and approaches for high-voltage spinel lithium-ion batteries, *ChemPhysChem*, 2014, **15**, 1940–1954.

4 J. Cabana, M. Casas-Cabanas, F. O. Omenya, N. A. Chernova, D. Zeng, M. S. Whittingham and C. P. Grey, Composition-structure relationships in the Li-ion battery electrode material $LiNi_{0.5}Mn_{1.5}O_4$, *Chem. Mater.*, 2012, **24**, 2952–2964.

5 B. Aktekin, M. Valvo, R. I. Smith, M. H. Sørby, F. Lodi Marzano, W. Zipprich, D. Brandell, K. Edström and W. R. Brant, Cation Ordering and Oxygen Release in $LiNi_{0.5-x}Mn_{1.5+x}O_{4-y}$ (LNMO): *In Situ* Neutron Diffraction and Performance in Li Ion Full Cells, *ACS Appl. Energy Mater.*, 2019, **2**, 3323–3335.

6 G. Q. Liu, L. Wen and Y. M. Liu, Spinel $LiNi_{0.5}Mn_{1.5}O_4$ and its derivatives as cathodes for high-voltage Li-ion batteries, *J. Solid State Electrochem.*, 2010, **14**, 2191–2202.

7 J. Liu, A. Huq, Z. Moorhead-Rosenberg, A. Manthiram and K. Page, Nanoscale Ni/Mn Ordering in the High Voltage Spinel Cathode $LiNi_{0.5}Mn_{1.5}O_4$, *Chem. Mater.*, 2016, **28**, 6817–6821.

8 Y. Chen, Y. Cheng, J. Li, M. Feygenson, W. T. Heller, C. Liang and K. An, Lattice-Cell Orientation Disorder in Complex Spinel Oxides, *Adv. Energy Mater.*, 2017, **7**, 1601950.

9 M. Casas-Cabanas, C. Kim, J. Rodríguez-Carvajal and J. Cabana, Atomic defects during ordering transitions in $LiNi_{0.5}Mn_{1.5}O_4$ and their relationship with electrochemical properties, *J. Mater. Chem. A*, 2016, **4**, 8255–8262.

10 J. Song, D. W. Shin, Y. Lu, C. D. Amos, A. Manthiram and J. B. Goodenough, Role of Oxygen Vacancies on the Performance of $Li[Ni_{0.5-x}Mn_{1.5+x}]O_4$ ($x = 0$, 0.05, and 0.08) Spinel Cathodes for Lithium-Ion Batteries, *Chem. Mater.*, 2012, **24**, 3101–3109.

11 D. Pasero, N. Reeves, V. Pralong and A. R. West, Oxygen Nonstoichiometry and Phase Transitions in $LiMn_{1.5}Ni_{0.5}O_{4-\delta}$, *J. Electrochem. Soc.*, 2008, **155**, A282.

12 J. Xiao, X. Chen, P. V. Sushko, M. L. Sushko, L. Kovarik, J. Feng, Z. Deng, J. Zheng, G. L. Graff, Z. Nie, D. Choi, J. Liu, J.-G. Zhang and M. S. Whittingham, High-performance $LiNi_{0.5}Mn_{1.5}O_4$ spinel controlled by Mn^{3+} concentration and site disorder, *Adv. Mater.*, 2012, **24**, 2109–2116.

13 G. Liang, V. K. Peterson, K. W. See, Z. Guo and W. K. Pang, Developing high-voltage spinel $LiNi_{0.5}Mn_{1.5}O_4$ cathodes for high-energy-density lithium-ion batteries: current achievements and future prospects, *J. Mater. Chem. A*, 2020, **8**, 15373–15398.

14 R. Kanno, M. Yonemura, T. Kohigashi, Y. Kawamoto, M. Tabuchi and T. Kamiyama, Synthesis and structures of lithium manganese oxide spinel, $LiMn_2O_{4-\delta}$ ($0 \leq \delta \leq 0.27$), *J. Power Sources*, 2001, **97–98**, 423–426.

15 M. Kunduraci and G. G. Amatucci, Effect of oxygen non-stoichiometry and temperature on cation ordering in $LiMn_{2-x}Ni_xO_4$ ($0.50 \geq x \geq 0.36$) spinels, *J. Power Sources*, 2007, **165**, 359–367.

16 R. D. Shannon, Revised Effective Ionic Radii and Systematic Studies of Interatomic Distances in Halides and Chalcogenides, *Acta Crystallogr.*, 1976, 751–767.
17 J. Cabana, H. Zheng, A. K. Shukla, C. Kim, V. S. Battaglia and M. Kunduraci, Comparison of the Performance of $LiNi_{1/2}Mn_{3/2}O_4$ with Different Microstructures, *J. Electrochem. Soc.*, 2011, **158**, A997.
18 L. Cai, Z. Liu, K. An and C. Liang, Unraveling structural evolution of $LiNi_{0.5}Mn_{1.5}O_4$ by *in situ* neutron diffraction, *J. Mater. Chem. A*, 2013, **1**, 6908.
19 S. Patoux, L. Daniel, C. Bourbon, H. Lignier, C. Pagano, F. Le Cras, S. Jouanneau and S. Martinet, High voltage spinel oxides for Li-ion batteries: From the material research to the application, *J. Power Sources*, 2009, **189**, 344–352.
20 A. Hofmann, A. Höweling, N. Bohn, M. Müller, J. R. Binder and T. Hanemann, Additives for Cycle Life Improvement of High-Voltage LNMO-Based Li-Ion Cells, *ChemElectroChem*, 2019, **6**, 5255–5263.
21 H. Liu, X. Zhang, X. He, A. Senyshyn, A. Wilken, D. Zhou, O. Fromm, P. Niehoff, B. Yan, J. Li, M. Muehlbauer, J. Wang, G. Schumacher, E. Paillard, M. Winter and J. Li, Truncated Octahedral High-Voltage Spinel $LiNi_{0.5}Mn_{1.5}O_4$ Cathode Materials for Lithium Ion Batteries: Positive Influences of Ni/Mn Disordering and Oxygen Vacancies, *J. Electrochem. Soc.*, 2018, **165**, A1886–A1896.
22 H. Liu, R. Kloepsch, J. Wang, M. Winter and J. Li, Truncated octahedral $LiNi_{0.5}Mn_{1.5}O_4$ cathode material for ultralong-life lithium-ion battery: Positive (100) surfaces in high-voltage spinel system, *J. Power Sources*, 2015, **300**, 430–437.
23 K. R. Chemelewski, D. W. Shin, W. Li and A. Manthiram, Octahedral and truncated high-voltage spinel cathodes: the role of morphology and surface planes in electrochemical properties, *J. Mater. Chem. A*, 2013, **1**, 3347.
24 T.-F. Yi, J. Mei and Y.-R. Zhu, Key strategies for enhancing the cycling stability and rate capacity of $LiNi_{0.5}Mn_{1.5}O_4$ as high-voltage cathode materials for high power lithium-ion batteries, *J. Power Sources*, 2016, **316**, 85–105.
25 J.-H. Kim, S.-T. Myung, C. S. Yoon, I.-H. Oh and Y.-K. Suna, Effect of Ti Substitution for Mn on the Structure of $LiNi_{0.5}Mn_{1.5-x}Ti_xO_4$ and Their Electrochemical Properties as Lithium Insertion Material, *J. Electrochem. Soc.*, 2004, A1911–A1918.
26 M.-L.-P. Le, P. Strobel, C. V. Colin, T. Pagnier and F. Alloin, Spinel-type solid solutions involving Mn^{4+} and Ti^{4+}:Crystal chemistry, magnetic and electrochemical properties, *J. Phys. Chem. Solids*, 2011, **72**, 124–135.
27 T. Ohzuku, K. Ariyoshi, S. Takeda and Y. Sakai, Synthesis and characterization of 5 V insertion material of Li $[Fe_yMn_{2-y}]O_4$ for lithium-ion batteries, *Electrochim. Acta*, 2001, 2327–2336.
28 G. B. Zhong, Y. Y. Wang, Y. Q. Yu and C. H. Chen, Electrochemical investigations of the $LiNi_{0.45}M_{0.10}Mn_{1.45}O_4$ (M = Fe, Co, Cr) 5V cathode materials for lithium ion batteries, *J. Power Sources*, 2012, **205**, 385–393.
29 A. Höweling, A. Stoll, D. O. Schmidt, H. Geßwein, U. Simon and J. R. Binder, Influence of Synthesis, Dopants and Cycling Conditions on the Cycling Stability of Doped $LiNi_{0.5}Mn_{1.5}O_4$ Spinels, *J. Electrochem. Soc.*, 2017, **164**, A6349–A6358.
30 A. Höweling, D. Stenzel, H. Gesswein, M. Kaus, S. Indris, T. Bergfeldt and J. R. Binder, Variations in structure and electrochemistry of iron- and titanium-doped lithium nickel manganese oxyfluoride spinels, *J. Power Sources*, 2016, **315**, 269–276.
31 M. Kunduraci and G. G. Amatucci, Synthesis and Characterization of Nanostructured 4.7 V $Li_xMn_{1.5}Ni_{0.5}O_4$ Spinels for High-Power Lithium-Ion Batteries, *J. Electrochem. Soc.*, 2006, A1345–A1352.
32 S. Brunauer, P. H. Emmett and E. Teller, Adsorption of Gases in Multimolecular Layers, *J. Am. Chem. Soc.*, 1938, 309–319.
33 P. Stüble, J. R. Binder and H. Geßwein, Tracing structural changes in energy materials: A novel multi sample capillary setup for in house powder X-ray diffraction, *Electrochem. Sci. Adv.*, 2021, e2100143.
34 H. M. Rietveld, A profile refinement method for nuclear and magnetic structures, *J. Appl. Crystallogr.*, 1969, **2**, 65–71.
35 J. F. Bérar and P. Lelann, E.s.d.'s and estimated probable error obtained in Rietveld refinements with local correlations, *J. Appl. Crystallogr.*, 1991, **24**, 1–5.
36 F. Menil, Systematic trends of the ^{57}Fe Mössbauer isomer shifts in (FeO_n) and (FeF_n) polyhedra. Evidence of a new correlation between the isomer shift and the inductive effect of the competing bond T–X (→ Fe) (where X is O or F and T any element with a formal positive charge), *J. Phys. Chem. Solids*, 1985, 763–789.
37 N. Kiziltas-Yavuz, M. Yavuz, S. Indris, N. N. Bramnik, M. Knapp, O. Dolotko, B. Das, H. Ehrenberg and A. Bhaskar, Enhancement of electrochemical performance by simultaneous substitution of Ni and Mn with Fe in Ni–Mn spinel cathodes for Li-ion batteries, *J. Power Sources*, 2016, **327**, 507–518.
38 M. Yavuz, N. Kiziltas-Yavuz, A. Bhaskar, M. Scheuermann, S. Indris, F. Fauth, M. Knapp and H. Ehrenberg, Influence of Iron on the Structural Evolution of $LiNi_{0.4}Fe_{0.2}Mn_{1.4}O_4$ during Electrochemical Cycling Investigated by *in situ* Powder Diffraction and Spectroscopic Methods, *Z. Anorg. Allg. Chem.*, 2014, **640**, 3118–3126.
39 J. Lee, C. Kim and B. Kang, High electrochemical performance of high-voltage $LiNi_{0.5}Mn_{1.5}O_4$ by decoupling the Ni/Mn disordering from the presence of Mn^{3+} ions, *NPG Asia Mater.*, 2015, **7**, e211.
40 W. Zhu, D. Liu, J. Trottier, C. Gagnon, J. Howe, A. Mauger, C. M. Julien and K. Zaghib, *In situ* Raman spectroscopic investigation of $LiMn_{1.45}Ni_{0.45}M_{0.1}O_4$ (M = Cr, Co) 5 V cathode materials, *J. Power Sources*, 2015, **298**, 341–348.
41 W. Li, B. Song and A. Manthiram, High-voltage positive electrode materials for lithium-ion batteries, *Chem. Soc. Rev.*, 2017, **46**, 3006–3059.
42 N. Amdouni, K. Zaghib, F. Gendron, A. Mauger and C. M. Julien, Structure and insertion properties of disordered and ordered $LiNi_{0.5}Mn_{1.5}O_4$ spinels prepared by wet chemistry, *Ionics*, 2006, **12**, 117–126.
43 D. W. Shin, C. A. Bridges, A. Huq, M. P. Paranthaman and A. Manthiram, Role of Cation Ordering and Surface

Segregation in High-Voltage Spinel $LiMn_{1.5}Ni_{0.5-x}M_xO_4$ (M = Cr, Fe, and Ga) Cathodes for Lithium-Ion Batteries, *Chem. Mater.*, 2012, **24**, 3720–3731.

44 Q. Zhong, A. Bonakclarpour, M. Zhang, Y. Gao and J. R. Dahn, Synthesis and Electrochemistry of $LiNi_xMn_{2-x}O_4$, *J. Electrochem. Soc.*, 1997, 205–213.

45 W. Bronger, H. Bade and W. Klemm, Zur Kenntnis der Niccolate der Alkalimetalle, *Z. Anorg. Allg. Chem.*, 1964, 188–200.

46 G. Prado, E. Suard, L. Fournes and C. Delmas, Cationic distribution in the $Li_{1-z}(Ni_{1-y}Fe_y)1 + zO_2$ electrode materials, *J. Mater. Chem.*, 2000, **10**, 2553–2560.

47 G. Prado, L. Fournes and C. Delmas, Mixed cobalt and iron substituted lithium nickelate: a structural and electrochemical study, *Solid State Ionics*, 2000, 19–30.

48 A. Bhandari and J. Bhattacharya, Review—Manganese Dissolution from Spinel Cathode: Few Unanswered Questions, *J. Electrochem. Soc.*, 2017, **164**, A106–A127.

49 W. Li, Y.-G. Cho, W. Yao, Y. Li, A. Cronk, R. Shimizu, M. A. Schroeder, Y. Fu, F. Zou, V. Battaglia, A. Manthiram, M. Zhang and Y. S. Meng, Enabling high areal capacity for Co-free high voltage spinel materials in next-generation Li-ion batteries, *J. Power Sources*, 2020, **473**, 228579.